Strain-rate sensitivity (SRS) behavior of P/M superalloys associated with steady-state DRX during hot compression process

Y.Q. Ning [a], B.C. Xie [a*], C. Zhou [a], H.Q. Liang [a], M.W. Fu [b]

[a] *School of Materials Science & Engineering, Northwestern Polytechnical University, Xi'an 710072, P.R. China*

[b] *Department of Mechanical Engineering, The Hong Kong Polytechnic University, Hung Hom, Kowloon, Hong Kong, P.R. China*

*CORRESPONDING AUTHOR:

Tel: +86 29 88493744

Fax: +86 29 88492642

E-mail: bcx0314@mail.nwpu.edu.cn; bcx0314@163.com (B.C. Xie)

ABSTRACT:

Strain-rate sensitivity (SRS) is an important parameter to describe the thermodynamic behavior in plastic deformation process. In present work, SRS behavior associated with steady-state DRX in P/M superalloys has been quantitatively investigated. Based on the theoretical derivation and microstructure observation, the SRS coefficient was employed to identify the deformation mechanism. Meanwhile, the corresponding relationship between SRS coefficient *m*, stress exponent *n* and deformation mechanisms has also been revealed. The stress exponent *n* in the Arrhenius constitutive model of P/M superalloys has also been calculated. There was a relatively stable stress exponent range (n=4~6), indicating that dislocation evolution behaves as a major hot deformation mechanism for P/M FGH4096 superalloy. In addition, Bergstrom model and Senkov model have been combined to estimate the SRS coefficient in steady-state DRX and the value of *m* maintains at 0.2–0.22, which was associated with microstructure evolution during high temperature deformation. Furthermore, SRS coefficient distribution map and power dissipation efficiency distribution map were constructed associated with microstructure evolution during hot deformation, which contribute to optimize the processing parameters.

KEY WORDS:

Strain-rate sensitivity behavior; Steady-state DRX; Microstructural characterization; Moderate-speed hot deformation; P/M superalloys

1. Introduction

Strain-rate sensitivity (SRS) is an important parameter in description of the thermodynamic behaviors in plastic deformation process [1]. During hot deformation, flow curves, dynamic softening (DRX in especial) and microstructure evolution vary greatly with strain rate, showing substantial SRS [2–4]. Due to the significance and complex effect, a lot of papers systematically discuss strain rate sensitivity behavior during hot plastic processing. Magee et al. [5] investigated the SRS of an Al-Mg alloy with bimodal grain size and the *m* value is found to have a non-monotonic dependence on the temperature with negative value at room temperature, which increases to the positive value at 110℃ and then decreases to the negative again at 200℃. In addition, L.J. Chen [6] studied the strain rate sensitivity of GH4049 superalloy under simple tension, fatigue and creep condition and found out that this alloy has an obvious strain rate sensitivity at the working temperature of 832℃. Furthermore, Y. Wang et al. [7] established a hyperbolic-sine type equation for 718 superalloy to express the dependence of peak stress on strain rate. They also verified that the DRX process of this alloy is accelerated in the low strain rate range. According to the investigation of Karimi et al. [8], the SRS of the AZ31 alloy was found to be significantly dependent on the deformation temperature, strain rate and imposed strain (the *m* value ranging from 0.08 to 0.24 at different deformation conditions.). Bianchi and Karjalainen [9] investigated the dynamic and metadynamic recrystallization behavior in bar rolling of DIN55Cr3 medium-carbon steel and developed a suitable constitutive model under the influence of Zener-Hollomon parameter by introducing strain rate sensitivity coefficient. As one of the most important structural materials, powder metallurgy (P/M) Ni-based superalloy is critical to the continuous

development of high-performance turbine engines. Owing to its excellent tensile and creep properties and microstructural stability at the temperature up to 750℃ for the extended exposure period [10], FGH4096 superalloy with a fine, homogenous and macrosegregation-free microstructure, is widely utilized to produce turbine disk. Due to the poor workability of the alloy, however, it is difficult to control its microstructure and then to optimize the final properties of products made of this superalloy. Thus, it is very necessary for FGH4096 to systematically investigate the strain rate sensitivity and combine it with DRX microstructure evolution.

This research is aimed at investigation on the strain-rate sensitivity behavior and the microstructure evolution of FGH4096 superalloy during hot deformation process with typical dynamic softening (DS) behavior and, steady-state DRX undergoing simultaneously. Two models proposed by Bergstorm [11] and Senkov [12] respectively were combined to estimate the strain rate sensitivity coefficient during steady-state DRX process. In addition, the SRS coefficient distribution and power dissipation efficiency distribution maps for hot deformation of P/M FGH4096 superalloy have been constructed from the m values in quantified characterization on steady-state DRX. And both of the two maps were then combined with the microstructures of the superalloy after deformation to investigate the microstructure evolution. Based on these new findings, the processing parameters were optimized for processing of P/M FGH4096 superalloy.

2. Materials and experimental procedures

FGH4096 powder used in this research was produced by plasma rotation electronic pole

(PREP). The main chemical composition (wt. %) of the experimental powder is: C, 0.02; Al, 2.2; W, 4.0; Nb, 0.8; Mo, 4.0; Ti, 3.7; Cr, 16.0; Co, 13.0; Ni-bal. The size of the nearly spherical powder is about 150μm (-100 mesh). The as-received FGH4096 bars were prepared by hot isostatic press (HIP, 1200℃/3h/120MPa). In order to homogenize the microstructure, the HIPed P/M FGH4096 superalloy were annealed at 1115℃ for 2h and air-cooled to room temperature prior to isothermal compression.

The prior-deformed microstructure of the P/M bars is shown in Fig.1, which obviously shows the existence of previous particle boundaries (PPBs) network. TEM examination of the specimens revealed the existence of as-cast γ` phase and the volume fraction of the γ` phase is estimated to be about 34% [10]. Cylindrical specimens with the diameter of 8mm and the height of 12mm were machined from the annealed bars for isothermal compression testing. The isothermal compression experiments were conducted on a Gleeble-1500D simulator. And five different temperatures (1020, 1050, 1080, 1110 and 1140℃) and four different strain rates (0.001, 0.01, 0.1 and $1s^{-1}$) were utilized. In order to ensure the complete heating and avoid undesired grain growth under high temperature, the specimens were heated with a heating rate of 10℃/s, and soaked for 5.0min at the deformation temperature prior to isothermal compression. The deformation temperature was controlled to ±2℃. The flow stress was automatically recorded as a function of strain and strain rate by the testing system. The specimens were deformed to 50% of their original height and were immediately water-quenched to keep the deformed microstructure. The deformed specimens were then sliced parallel to the compression axis for microstructural analysis by optical microscope (OM) and transmission electron microscopy (TEM).

Fig.1 is around here.

3. Results and discussion

3.1 Typical flow behavior of P/M superalloys

Fig.2 shows the selected flow curves of P/M FGH4096 superalloy compressed at different strain rates and deformation temperature of 1080 and 1110℃, respectively. It is found that the ideal flow curves can be divided into three typical stress variation stages, i.e., working-hardening state, continuous softening state and steady flowing state. As shown in the flow curve, the flow stress rapidly increases to the peak stress in the working-hardening stage for dislocation proliferation and continuous trapping by existing obstacles. Then, a very obvious stress softening from the peak stress is observed in almost all the curves except for the two curves with a lower strain rate at the deformation temperature of 1110℃, indicating the occurrence and onset of DRX under hot deformation from the traditional qualitative view [13]. Due to the limited effect of diffusion, only the curves with a lower strain rate, such as 0.001, 0.01 and $0.1s^{-1}$, and higher deformation temperature, such as 1080, 1110 and 1140℃, obviously exhibits a steady trend with a steady state stress for continuous softening effect. For those flow curves with higher strain rate and lower temperature, the softening effect was restrained due to insufficient diffusion, and thus the steady state between working-hardening and dynamic softening effects could not be reached easily. The variation of the steady state stress with deformation temperature and strain rate is presented in Fig.2c and Fig.3a, respectively. In general, both of the deformation temperature and strain

rate influence the steady state stress significantly.

Fig.2 is around here.

It is acknowledged that microstructural evolution mechanisms reveal a significant sensitivity to the deformation condition. When the deformation is conducted at low temperature, it is under the control of the thermal activation on dislocation motion, such as single-slipping, climbing and cross-slipping. With the increase of temperature, the interaction between dislocation and vacancy benefits the hot deformation under the sufficient diffusion effect. With the hot deformation undergoing at high temperature and low strain rate, the grain boundary sliding (GBS) and its accommodation process are the major mechanisms for superplastic deformation [14]. The flow characteristics of the hot deformation demonstrate a strong dependence on the competition between work-hardening and dynamic softening induced by DRX and/or DRV. The SRS measurements were employed to identify the change of deformation mechanisms [15]. The correspondence between the deformation microstructural mechanisms and the suitable Arrhenius constitutive models is given in Table 1. A clear corresponding relationship between the stress exponents n, the reciprocal of m values, and the deformation mechanisms are summarized in this table [16–20].

Table 1 is around here.

As shown in Fig.3a, the stress exponent n for hot deformation of FGH4096 superalloy

under different temperatures are calculated based on the Arrhenius constitutive model. Fig.3b shows the relationship between the stress exponent and deformation evolution microstructural mechanism. There is a relatively stable stress exponent range, from 4 to 6, indicating dislocation evolution behaves as a major mechanism for hot deformation of P/M FGH4096 superalloy.

Fig.3 is around here.

3.2 Strain rate sensitivity behavior associated with steady-state DRX

Work-hardening and dynamic-softening during the hot plastic deformation for metallic materials have a strongly interdependence on the co-existence and competition between dislocation proliferation and annihilation. As shown in Fig.2, the flow stress rapidly increases to the peak stress in the working-hardening stage for dislocation proliferation and continuous trapping by existing obstacles. The obvious stress softening from the peak stress is then easily observed for the dislocation density drop by dislocation offsetting with the opposite sign and rearrangement with the same [21]. Finally, a relatively steady state could be reached in those curves with higher temperature and lower strain rate. It is the dislocation evolution that plays a significant role in all these processes [22]. Therefore, the characterization of the dislocation density variation during the hot compression is essential for investigation on the optimization of hot forging process of P/M superalloys.

3.2.1 Approach of strain rate sensitivity behavior

Basing on the investigation on the interaction between the mobile and pinned dislocations,

Bergstrom [23] proposed a dynamic model to describe the dislocation density variation in the following

$$\frac{\partial \rho}{\partial \varepsilon} = U - \Omega \rho \tag{1}$$

where U and Ω denote the dislocation proliferation and the annihilation coefficient, respectively.

With this model, the dislocation density variation can be simply described as

$$\left(\frac{\partial \rho}{\partial \varepsilon}\right)_t = \left(\frac{\partial \rho_A}{\partial \varepsilon}\right)_t + \left(\frac{\partial \rho_p}{\partial \varepsilon}\right)_t \tag{2}$$

where $\left(\frac{\partial \rho_A}{\partial \varepsilon}\right)_t$ and $\left(\frac{\partial \rho_p}{\partial \varepsilon}\right)_t$ denote the rates of dislocation annihilation and proliferation, respectively.

According to the model proposed by Senkov [24], the rate of dislocation annihilation can been represented as:

$$\left(\frac{\partial \rho}{\partial t}\right)_\varepsilon = -\rho d_{GB} v_{GB} \tag{3}$$

where ρ (m^{-2}), d_{GB} (m^{-1}) and v_{GB} (m/s) denote the dislocation density, the grain boundary density (the area of grain boundaries per unit volume) and the mean migration rate of the grain boundaries, respectively. With the introduction of strain rate $\dot{\varepsilon}$, Eq. (3) can be further formulated as:

$$\left(\frac{\partial \rho_A}{\partial \varepsilon}\right)_t = \left(\frac{\partial \rho}{\partial \varepsilon}\right)_t = -\frac{1}{\dot{\varepsilon}} \cdot \rho d_{GB} v_{GB} \tag{4}$$

Otherwise, the relationship between the mean grain size and the steady state stress can be described by the following empirical Eq. (5):

$$D = Ab\left(\frac{G}{\sigma}\right)^{p} \tag{5}$$

where A a material constant and p=1.5–2.0 for most metals and alloys [25, 26]. It is assumed that the grains are spherical shape, the grain boundary density d_{GB} is calculated as:

$$d_{GB} = \frac{6}{Ab}\left(\frac{\sigma}{G}\right)^{p} \tag{6}$$

Subsequently, if M_{GB} ($m^4/J \cdot s$) represents the grain boundary mobility and F (Pa) denotes the driving force for grain boundary migration, the average migration rate of the grain boundaries can be expressed as [27]

$$v_{GB} = M_{GB}F \tag{7}$$

The grain boundary mobility is usually assumed to be proportional to the self-diffusivity at grain boundaries and can be calculated by the following equation proposed by Tnrnbull [28]:

$$\begin{cases} M_{GB} = \dfrac{\beta\delta D_{GB}V_m}{b^2RT} \\ D_{GB} = D_0 \cdot \exp\left(-\dfrac{Q}{RT}\right) \end{cases} \tag{8}$$

where δ, D_{GB}, Q and V_m represent the grain boundary thickness, the self-diffusivity along a grain boundary, the activation and the molar volume, respectively. And β denotes the fraction parameter with the estimated value of 0.1–0.5 [29].

Moreover, the driving force for migration can be described as

$$F = \frac{1}{2}Gb^2\rho \tag{9}$$

where G is the shear modulus of the deformation materials.

With the combination of Eqs.(4, 6–9), the rate of dislocation annihilation is obtained as

$$\left(\frac{\partial \rho_A}{\partial \varepsilon}\right)_t = \left(\frac{\partial \rho}{\partial \varepsilon}\right)_t = -\frac{1}{\dot{\varepsilon}} \cdot \frac{3GV_m \beta \delta \rho^2}{ARTb} \cdot \left(\frac{\sigma}{G}\right)^p \cdot D_0 \cdot \exp\left(-\frac{Q}{RT}\right) \tag{10}$$

In addition, the rate of dislocation proliferation owing to wok hardening can be described as

$$\left(\frac{\partial \rho}{\partial \varepsilon}\right)_t = \frac{2}{bL} \tag{11}$$

where b is the Burgers vector and L the mean free slip distance. Free slip distance L is related to the existence of encountered obstacles, such as grain boundaries, strengthening phases and other dislocations [9]. According to the parallel operation of force, the free slip distance L for dislocation migration during the hot deformation of metallic materials is formulated expressed as [30]

$$\frac{1}{L} = \frac{1}{D} + \frac{1}{d} + \frac{1}{t} \tag{12}$$

where D, d and t represent the mean grain size, the space between the adjacent dislocations and second the phase size, respectively. As shown in Fig.1, for the experimental material FGH4096 superalloy, the grain size of the as-received material (30μm) and the strengthening γ' phase (1.5μm) are both much larger than the distance between the adjacent dislocations (10nm). Therefore, the influence of grain size and the second phase can be neglected, and thus the free distance the dislocation can migrate is approximately equal to the space between adjacent dislocations, i.e. $L=d$. During the initial stage of plastic deformation, the originally existing dislocations develop the Orowan circles to proliferate mobile ones to continue the deformation [31]. The distance between the dislocations will be shortened with the increase of density. With the assumption of the uniform distribution of dislocation, the dislocation spacing could be considered as a function of density [32]:

$$d = \frac{1}{\sqrt{\rho}} \tag{13}$$

Substituting Eqs.(12) and (13) into Eq.(11), the dislocation proliferation rate can be determined as

$$\left(\frac{\partial \rho_p}{\partial \varepsilon}\right)_t = \left(\frac{\partial \rho}{\partial \varepsilon}\right)_t = \frac{2\sqrt{\rho}}{b} \tag{14}$$

On the other hand, the flow stress of material is linked to the dislocation density according to the following Taylor relation [33]:

$$\sigma = \alpha G M b \sqrt{\rho} \tag{15}$$

where α is Taylor constant with the value of about 0.5 and G is the shear modulus. M represents the conversion factor from shear to normal deformation with the value of 3.06 and b is the Burgers vector.

It is believed the increase of dislocation density is attributed to the continuous straining with the collision probability and the increase of internal distortion energy. With the critical condition satisfied, the annihilation and proliferation of dislocations could be accelerated spontaneously to reestablish a steady state:

$$\left(\frac{\partial \rho}{\partial \varepsilon}\right)_t \Big|_{ss} = \left(\frac{\partial \rho_A}{\partial \varepsilon}\right)_t + \left(\frac{\partial \rho_P}{\partial \varepsilon}\right)_t = 0 \tag{16}$$

By substituting Eqs. (10), (14) and (15) into Eq. (16), a simple function with a certain physical meaning is obtained in Arrhenius power-type function in the following:

$$\dot{\varepsilon} = A \cdot \sigma^{4.5\sim5} \cdot \exp\left(-\frac{Q}{RT}\right) \tag{17}$$

where the constant term $A = \frac{3}{2} \cdot \frac{\beta \delta V_m D_0}{ART\alpha^3 M^3 b^3 G^{4.5\sim5}}$.

Furthermore, the stress exponent range of 4.5~5 and corresponding range of m value from

0.2 to 0.22 during steady-state DRX can be easily obtained from Eq. (17). The *m* value not only is consistent with the values determined from Fig.3a, but also has an excellent agreement with other experiment results by using different metal materials, as shown in Table 2 [34–39].

Table 2 is around here.

3.2.2 Change of strain rate sensitivity coefficient

Based on the flow stress data from the isothermal compression of FGH4096 superalloy, the SRS coefficient for a certain deformation condition was determined by spline fitting of the flowing equation at the same temperature:

$$\sigma = k \cdot \dot{\varepsilon}^{m} \tag{18}$$

In order to reveal the influence of SRS on microstructural evolution, the SRS value distribution map with the strain of 0.65 in hot deformation of FGH4096 superalloy was constructed and shown in Fig.4 with corresponding typical microstructure. It can be clearly observed that m value over 0.2 is located at right lower domain of the contour line map except for the two special regimes with the abnormal *m* value, marked by ellipses in the figure. The regime marked by red ellipse can be considered as the result of instability, which can be verified by the instability criterion given by the red curve, obtained from the instability map, in the contour line map. The instability regime, existing with the strain rate of greater than $0.1s^{-1}$, indicates the higher possibility of unstable flow. As shown in Fig.4a, a distinct adiabatic shear band (ASB) marked with a red arrow is observed in the matched

microstructures, revealing the existence of the strong partial flow and thus results in the increase of *m* value under the condition with low deformation temperature and high strain rate. Another special regime with the high *m* value, marked by black ellipse at the lower left corner, occurs at the condition with the temperature of 1020–1050℃ and the strain rate of about 0.001–0.002s^{-1}. According to the investigation of W.D. Zeng et al., [40] superplasticity is characterized by high power dissipation efficiency (>60%), and the power dissipation efficiency increases rapidly with the decrease of strain rate. Therefore, as shown in Fig.5, this special regime can be reasonably considered as the result of superplasticity.

Fig.4 is around here.

Fig.5 is around here.

In Fig.4, according to previous calculation, the regime marked by blue ellipse is considered as the region of DRX for FGH4096 during hot deformation process, which is confined to the temperature of 1050–1140℃ and the strain rate of 0.001–0.1s^{-1} except for the right bottom corner. In dynamic material model (DMM), the total power *p* dissipated during hot deformation process can be designed as:

$$P = \sigma \cdot \dot{\varepsilon} = \int_0^{\dot{\varepsilon}} \sigma d\dot{\varepsilon} + \int_0^{\sigma} \dot{\varepsilon} d\sigma = G + J \qquad (19)$$

where *G* content represents the power dissipated by plastic deformation, which is mostly converted to heat and the other power, *J* content, is absorbed by the deformed specimen to maintain the microstructural evolution. Power dissipation efficiency represents the energy fraction absorbed by the deformation material, and is defined as a function of SRS value

[41]:

$$\eta = \frac{J}{J_{\max}} = \frac{2m}{m+1} \tag{20}$$

It has been widely acknowledged that more energy is necessary to maintain the microstructural evolution during DRX process and, thus, a large power dissipation efficiency occurs at the region where DRX take places. Power dissipation efficiency distribution map for the hot deformation of FGH4096 with the strain of 0.65 is established and shown in Fig.5. It can be distinctly observed that the region with a large power dissipation efficiency indicating the occurrence of DRX is defined to moderate temperature and lower strain rate, which is consistent with the result from the *m* values distribution map in presented Fig.4.

On the other hand, several typical corresponding microstructures of the region where DRX occurs are shown in Fig.4b–h. Fig.4b–d present the microstructures at the temperature of 1050℃ and the strain rate of 0.1, 0.01 and 0.001s^{-1}, respectively. All of them consist of ultrafine recrystallization nucleus and coarse grains undergoing hot deformation, which is verified distinctly in TEM image. As shown in Fig.4e, the obvious recrystallization nucleus is easily found at the grain boundaries even at the low strain rate of 0.001s^{-1}, indicating that the incomplete recrystallization is resulted from the insufficient driving force instead of the lack of time. Therefore, the temperature of 1050 ℃ may be appropriate for GHF4096 superalloy to nucleate during hot deformation, which has less sensitivity to the strain rate ranged from 0.001–0.1s^{-1}. As shown in Fig.4g and h, grains undergoing DRX in the samples deformed at the temperature of 1140 ℃ and the strain rate of 0.1 and 0.01s^{-1} are found coarsened strongly, which is almost closed to the size of the previous grains. Moreover, a

typical microstructure undergoing complete DRX (1080℃ and $0.01s^{-1}$, for example) consists of equiaxed grains with straight and clean grain boundaries, as shown in Fig.4f.

Therefore, with the SRS coefficient distribution map, an optimized regime, where microstructure could be consisting of fine equiaxed recrystallization grains, the FGH4096 superalloy during steady state can be mainly confined to the temperature of 1080–1110℃ and the strain rate of $0.1–0.001s^{-1}$. In order to discuss more conveniently, the selected microstructure matched *m* values are given in Fig.6, in which all of them consist of equiaxed recrystallization grains and the main difference is the grain size. It can be obviously observed that the recrystallization grain size increases with the decrease of strain rate at the temperature both of 1080 and 1110℃. It is the different coarsening velocity at different temperatures that is of concern. The γ' phase is believed to have a strong influence on the microstructure of FGH4096 superalloy. On the other hand, the deformation time become long with the decrease of strain rate, leading to the various fractions of strengthening phase γ'. As shown in Fig.6a–c, due to the existence of more phase γ', the growth of recrystallization grains is restrained effectively when it is deformed at 1080℃ (below γ' phase solution temperature), thus, revealing a less sensitivity to strain rate. However, when it is deformed at 1110℃ (very closed to γ' phase solution temperature), the recrystallization grains become coarsened rapidly with the decrease of strain rate for the solution of most γ' phase, as shown in Fig.6d–f. Therefore, a simple conclusion can be drawn that the microstructures of FGH4096 superalloy undergoing DRX are more sensitive to strain rate at or over the γ' phase solution temperature. Furthermore, based on the analysis above, the excellent microstructure of FHG4096 superalloy is obtained when the superalloy is

deformed in the region with the strain rate from 0.01 to 0.1s^{-1} and the temperatures from 1080 to 1110℃, and the strain rate should be elevated reasonably with the increase of deformation temperature.

Fig.6 is around here.

4. Conclusions

Strain rate sensitivity (SRS) associated with steady-state DRX in the hot deformation of FGH4096 P/M superalloy with previous particle boundary was quantitatively investigated through isothermal compression. Based on theoretical derivation and microstructure observation, the following conclusions are drawn:

(1) The SRS coefficient was employed to identify the deformation mechanism of FGH4096 P/M superalloy, and the corresponding relationship among SRS coefficient *m*, stress exponent *n*, and the deformation mechanism is established, which contributes to further optimization of the processing parameters for this alloy.

(2) The stress exponent *n* for processing P/M superalloy was calculated based on Arrhenius constitutive model. There is a relatively stable stress exponent range (n=4~6) indicating the dislocation evolution behaves as a major mechanism for hot deformation of P/M FGH4096 superalloy.

(3) Bergstrom and Senkov models were combined to estimate the SRS coefficient for steady-state DRX and *m* value is kept at 0.2–0.22. The relevant *m* values are associated with microstructure evolution during high temperature deformation.

(4) SRS coefficient distribution map and power dissipation efficiency distribution map were constructed associated with microstructure evolution during hot deformation, which contribute to optimize the processing parameters of FGH4096 P/M superalloy. And the optimum parameters for processing this superalloy are at the deformation temperature of 1080–1110℃ with the strain rate of 0.01–0.1s^{-1}. Meanwhile, the strain rate should be elevated reasonably with the increase of deformation temperature.

Acknowledgements

The work was financially supported by the National Natural Science Foundation of China (Grant No. 51101119) and China Postdoctoral Science Foundation (Grant No. 2015M570851). Also, Dr. Y.Q. Ning would like to thank the funding support by the Hong Kong Scholar Program (Grant No. XJ2014047) in The Hong Kong Polytechnic University.

References

[1] Y. Wang, Y. Liu, J.T. Wang, *Mater. Sci. Eng. A* **635**, 86 (2015).

[2] J.E. Jin, Y.K. Lee, *Acta Mater.* **60**, 1680 (2012).

[3] H.K. Yang, Z.J. Zhang, F.Y. Dong, Q.Q. Duan, Z.F. Zhang, *Mater. Sci. Eng. A* **607**, 551 (2014).

[4] S. Curtze, V.T. Kuokkala, *Acta Mater.* **58**, 5129 (2010).

[5] A.C. Magee, L.Ladani, *Mater. Sci. Eng. A* **582**, 276 (2013).

[6] L. Chen, *Mater. Sci. Eng. A* **527**, 1120 (2010).

[7] Y. Wang, W.Z. Shao, L. Zhen, L. Yang, X.M. Zhang, *Mater. Sci. Eng. A* **497,** 479 (2008).

[8] E. Karimi, A. Zarei-Hanzaki, M.H. Pishbin, H.R. Abedi, P. Changizian, *Mater. Des.* **49**, 173 (2013).

[9] J.R. Klepaczko, *Nucl. Eng. Des.* **127**, 103 (1991).

[10] Y. Ning, Z. Yao, H. Li, H. Guo, Y. Tao, Y. Zhang, *Mater. Sci. Eng. A* **527**, 961 (2010).

[11] F. Chen, K. Qi, Z. Cui, X. Lai, *Comput. Mater. Sci.* **83**, 331 (2014).

[12] O.N. Senkov, J.J. Jonas, F.H. Froes, *Mater. Sci. Eng. A* **255**, 49 (1998).

[13] Y.C. Lin, X.M. Chen, D.X. Wen, *Comput. Mater. Sci.* **83**, 282 (2014).

[14] J.S. Kim, J.H. Kim, Y.T. Lee, C.G. Park, C.S. Lee, *Mater. Sci. Eng. A* **263**, 272 (1999).

[15] R. Korla, A.H. Chokshi, *Scripta Mater* **63**, 913 (2010).

[16] A. K. Mukherjee, J. E. Bird, J. E. Dorn, *Trans. Am. Soc. Met.* **62**, 155 (1969).

[17] T.G. Langdon, *Philos. Mag.* **22**, 689 (1970).

[18] M. F. Ashby, R. A. Verrall, *Acta Metall.* **21**, 149 (1973).

[19] C. Herring, *J. Appl. Phys.* **21**, 437 (1950).

[20] R.L. Coble, *J. Appl. Phys*. **34**, 1679 (1963).

[21] R.C. Picu, *Acta Mater.* **52**, 3447 (2004).

[22] A. Nakatani, *Proc. Eng.* **10**, 1047 (2011).

[23] Y. Bergstrom, *Mater. Sci. Eng. A* **5**, 193 (1970).

[24] O. Senkov, J.J. Jonas, F.H. Froes, *Mater. Sci. Eng A* **255**, 49 (1998).

[25] H.J. McQueen, J. J. Jonas, *Plastic Deformation of Metals*, pp. 393, Academic Press, New York (1975).

[26] C.M. Sellars, *Phil. Trans. R. Soc. Lond*. **288**, 147 (1978).

[27] D. Turnbull, *J. Met.* **3**, 661 (1951).

[28] Y.V.R.K. Prasad, K.P. Rao, *Philos. Mag.* **84**, 3039 (2004).

[29] C.R. Hutchinson, H.S. Zurob, S.W. Sinclair, Y. Brechet, *Scripta Mater.* **59**, 635 (2008).

[30] Y. Estrin, H. Mecking, *Acta Metall.* **32**, 57 (1984).

[31] G.E. Dieter, *Mechanical Metallurgy*, pp. 145–150, McGraw-Hill, New York (1988).

[32] E.I. Galindo-Nava, P.E.J. Rivera-Diaz-del-Castillo, *Acta Mater.* **60**, 4370 (2012).

[33] A. Momeni, G.R. Ebrahimi, M. Jahazi, P. Bocher, *J. Alloys Comp.* **587**, 199 (2014).

[34] Y.C. Lin, J. Deng, Y.Q. Jiang, D.X. Wen, G. Liu, *Mater. Des.* **55**, 949 (2014).

[35] K. Wang, M.Q. Li, J. Luo, C. Li, *Mater. Sci. Eng. A* **528**, 4723 (2011).

[36] C.M. Sellars, W.J.McG. Tegart, *Mem. Sci. Rev. Metall.* **63**, 731 (1966).

[37] S. Venugopal, S.L. Mannan, Y.V.R.K. Prasad, *Mater. Sci. Eng. A* **117**, 143 (1994).

[38] H.B. Zhang, K.F. Zhang, Z. Lu, C.H. Zhao, X.L. Yang, *Mater. Sci. Eng. A* **604**, 1 (2014).

[39] Y. Wang, W.Z. Shao, L. Zhen, B.Y. Zhang, *Mater. Sci. Eng. A* **528**, 3218 (2011).

[40] W.D. Zeng, Y.G. Zhou, J. Zhou, H.Q. Yu, X.M. Zhang, *Rare Metal Mater. Eng.* **35**, 673 (2006).

[41] Y.V.R.K. Prasad, H.L. Gegel, S.M. Doraivelu, J.C. Malas, J.T. Morgan, *Metall. Trans. A* 15, 1883 (1984).

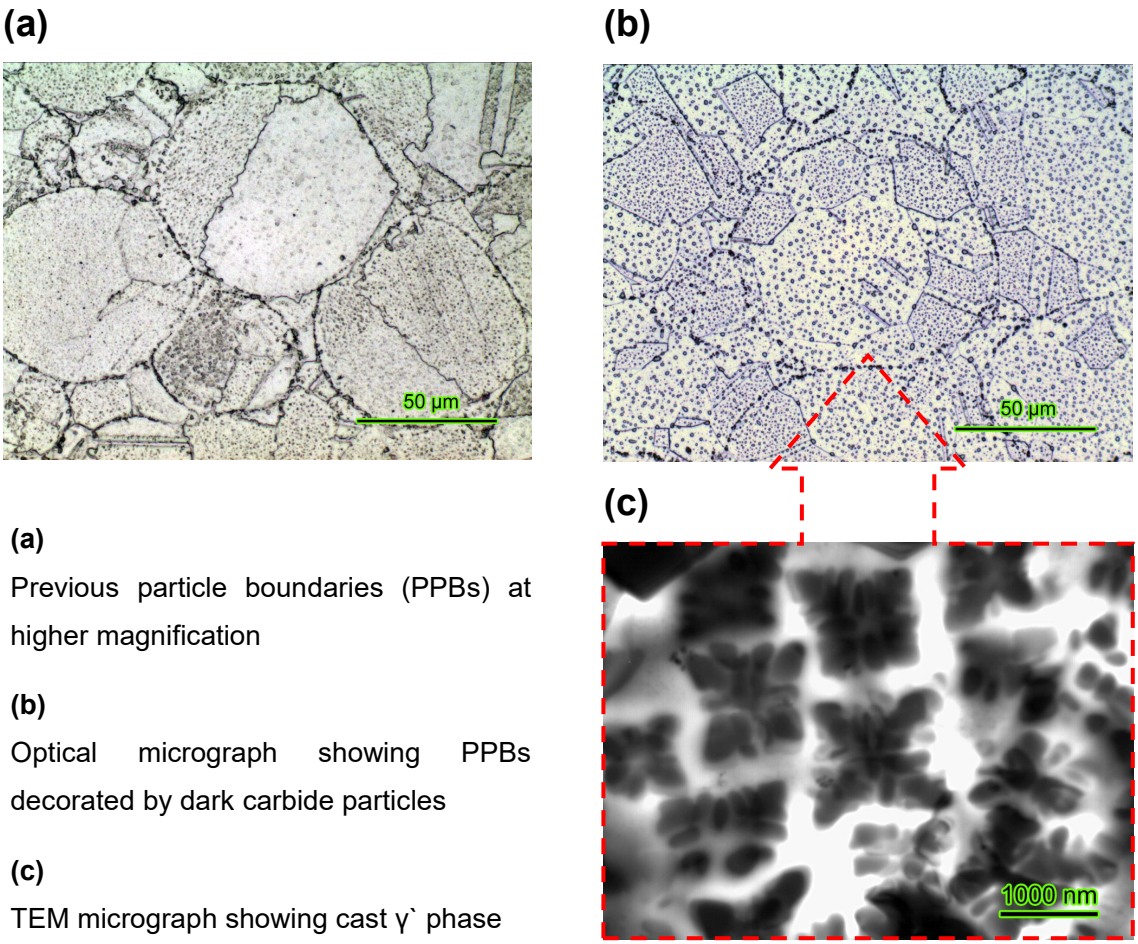

(a)

Previous particle boundaries (PPBs) at higher magnification

(b)

Optical micrograph showing PPBs decorated by dark carbide particles

(c)

TEM micrograph showing cast γ` phase

Fig.1 Typical microstructures of FGH4096 superalloy processed after pre-annealing treatment at 1150℃ for 2h and air-cooled to room temperature, which obviously revealing previous particle boundaries (PPBs) by dark carbide particles and cast γ` phase at higher magnification.

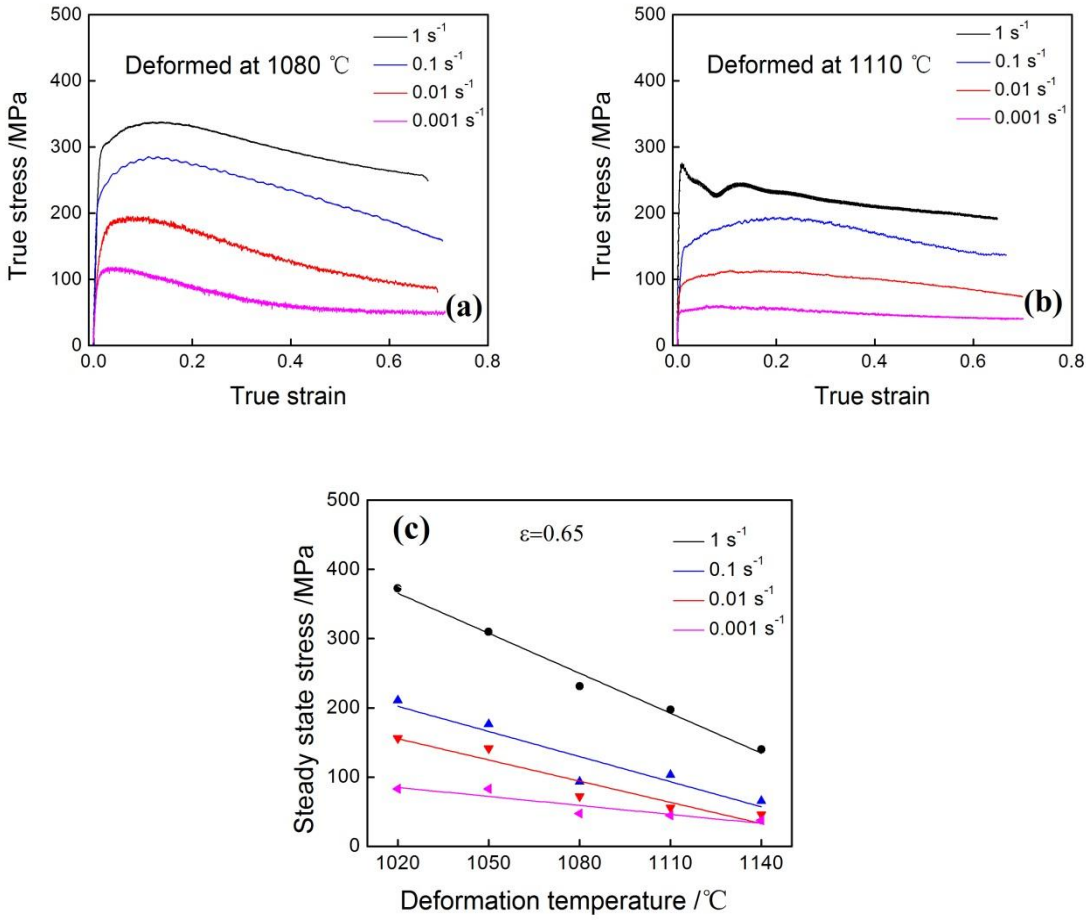

Fig.2 (a) and (b) Selected flow curves for FHG4096 superalloy under different deformation conditions obtained from isothermal compression experiments, and (c) the effect of deformation temperature on steady state stress.

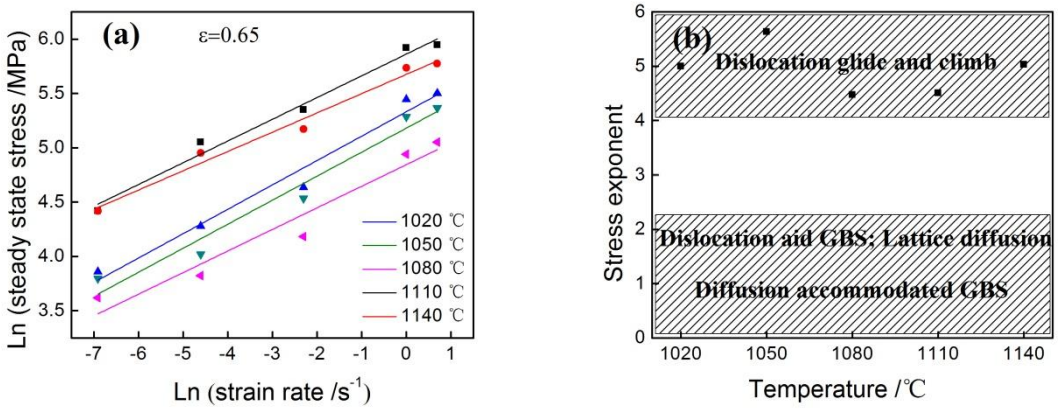

Fig.3 (a) Linear regression between Ln $\dot{\varepsilon}$ and Lnσ with the slope defined as stress exponent for hot deformation of FGH4096 superalloy under different temperatures, and (b) relationship among stress exponent, deformation temperatures and mechanisms.

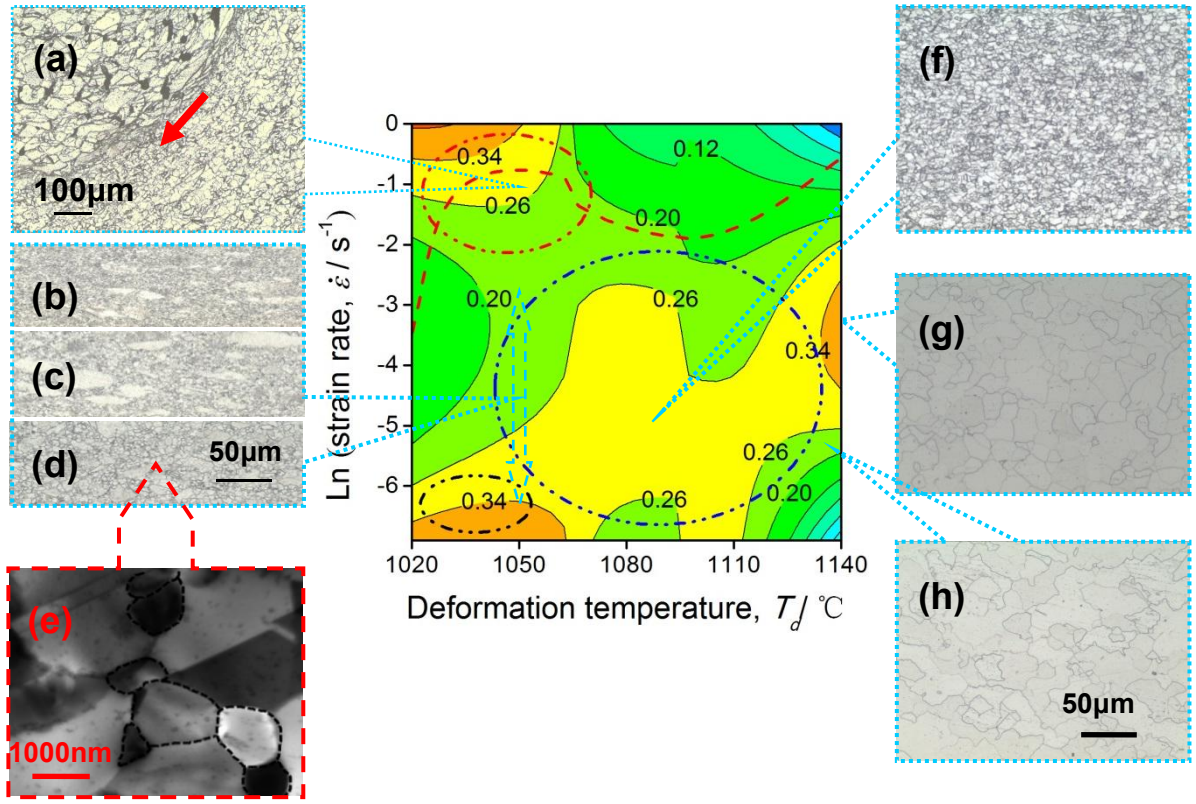

Fig.4 SRS coefficient distribution map illustrated by the selected microstructures for hot deformation of FGH4096 superalloy at true strain of 0.65.

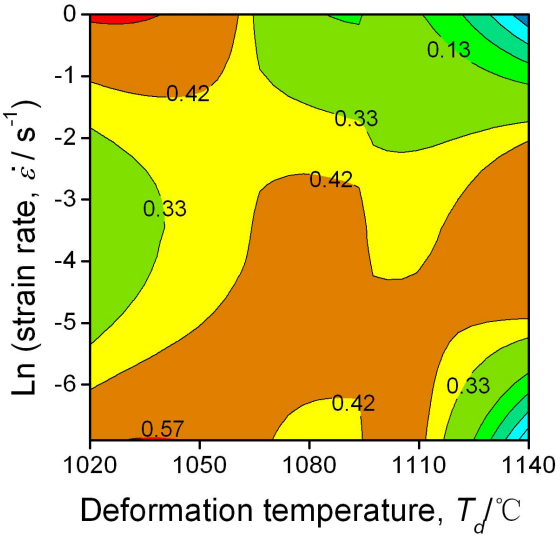

Fig.5 Power dissipation efficiency distribution map for hot deformation of FGH4096 superalloy at the true strain of 0.65.

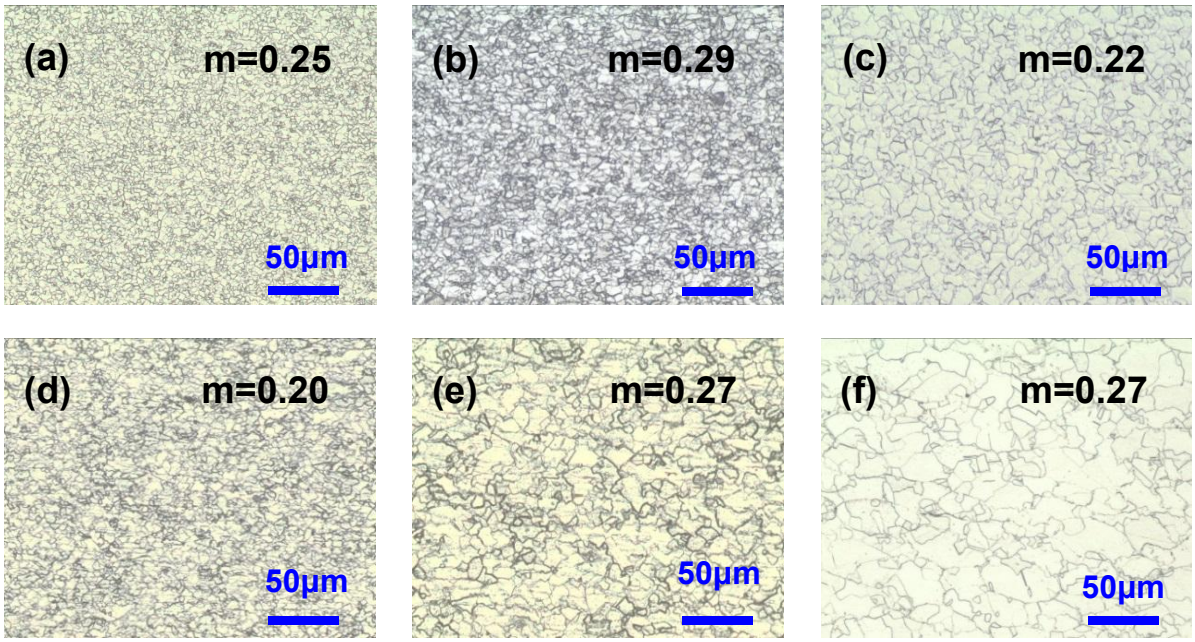

Fig.6 Typical microstructures of FGH4096 superalloy with m values of 0.2–0.3 processed after isothermal compression under different processing conditions:
(a) 1080℃/0.1s-1, (b) 1080℃/0.01s-1, (c) 1080℃/0.001s-1,
(d) 1110℃/0.1s-1, (e) 1110℃/0.01s-1, (f) 1110℃/0.001s-1.